Flexible, foldable, actively multiplexed, high-density electrode array for mapping brain activity *in vivo*

Jonathan Viventi[1,2,13], Dae-Hyeong Kim[3,13], Leif Vigeland[4], Eric S Frechette[5], Justin A Blanco[6], Yun-Soung Kim[7], Andrew E Avrin[8], Vineet R Tiruvadi[9], Suk-Won Hwang[7], Ann C Vanleer[9], Drausin F Wulsin[9], Kathryn Davis[5], Casey E Gelber[9], Larry Palmer[4], Jan Van der Spiegel[8], Jian Wu[10], Jianliang Xiao[11], Yonggang Huang[12], Diego Contreras[4], John A Rogers[7] & Brian Litt[5,9]

Arrays of electrodes for recording and stimulating the brain are used throughout clinical medicine and basic neuroscience research, yet are unable to sample large areas of the brain while maintaining high spatial resolution because of the need to individually wire each passive sensor at the electrode-tissue interface. To overcome this constraint, we developed new devices that integrate ultrathin and flexible silicon nanomembrane transistors into the electrode array, enabling new dense arrays of thousands of amplified and multiplexed sensors that are connected using fewer wires. We used this system to record spatial properties of cat brain activity *in vivo*, including sleep spindles, single-trial visual evoked responses and electrographic seizures. We found that seizures may manifest as recurrent spiral waves that propagate in the neocortex. The developments reported here herald a new generation of diagnostic and therapeutic brain-machine interface devices.

The utility of high-resolution neural recordings from the cortical surface for basic research and clinical medicine has been shown for a wide range of applications. Spatial spectral analysis of electrocorticograms (ECoGs) from the superior temporal gyrus and motor cortex has revealed that electrode spacing should be 1.25 mm or closer in humans to sufficiently capture the rich spatial information that is available[1]. Motor control signals[2] and spoken words[3] can be decoded with substantially improved performance using electrodes spaced 1 mm apart or less. In occipital cortex, arrays with 500-µm spacing have demonstrated micro-field evoked potentials that can distinguish ocular dominance columns[4]. The spatial scale for some pathologic signals is also submillimeter, based on observations of microseizures, microdischarges and high-frequency oscillations in epileptic brain[5,6].

However, the subdural electrodes in use clinically, for example, in the diagnosis and treatment of epilepsy, are much larger (~3 mm in diameter) and have large interspacing (~10 mm) because of the clinical need to record from large areas of the brain surface (80 mm × 80 mm) to accurately localize seizure-generating brain regions. Large area electrode arrays with high spatial resolution are also needed in brain-machine interface (BMI) applications to account for variability in the location of brain functions, which can vary by ~5 mm across subjects[7-10]. High-resolution interface over a large area has previously been impossible owing to the infeasibility of connecting thousands of wires in the small intracranial space.

Much of the existing research in electrode technology has focused on penetrating electrode arrays, such as the Utah array[11], which can provide a high-resolution interface to a small area of cortex and enable high-performance neuromotor prostheses[12]. However, arrays of penetrating microelectrodes may only function for 6–12 months[13] before the signal quality on most electrodes becomes substantially diminished. These devices can also cause hemorrhage and inflammatory tissue responses from the immediate insertion[14,15] and over long periods of time, possibly as a result of the inability of the rigid penetrating electrodes to flex and move as the brain pulses, swells and contracts[16].

Highly flexible arrays of subdural electrodes have unique advantages over penetrating microelectrode arrays in that they are able to maintain signal quality over extended periods of time with minimized irritation and injury to brain tissues[17–19]. Furthermore, the micro-electrocorticographic (µECoG) signal recorded from flexible arrays of nonpenetrating electrodes with high-resolution can provide comparable information content to the spiking activity recorded by penetrating microelectrodes in some applications, such as BMI[20–22].

[1]Department of Electrical and Computer Engineering, Polytechnic Institute of New York University, Brooklyn, New York, USA. [2]Center for Neural Science, New York University, New York, New York, USA. [3]School of Chemical and Biological Engineering, Seoul National University, Seoul, Korea. [4]Department of Neuroscience, University of Pennsylvania School of Medicine, Philadelphia, Pennsylvania, USA. [5]Penn Epilepsy Center, Department of Neurology, Hospital of the University of Pennsylvania, Philadelphia, Pennsylvania, USA. [6]Department of Electrical and Computer Engineering, United States Naval Academy, Annapolis, Maryland, USA. [7]Department of Materials Science and Engineering, Beckman Institute for Advanced Science and Technology and Frederick Seitz Materials Research Laboratory, University of Illinois at Urbana-Champaign, Urbana, Illinois, USA. [8]Department of Electrical and Systems Engineering, University of Pennsylvania, Philadelphia, Pennsylvania, USA. [9]Department of Bioengineering, University of Pennsylvania, Philadelphia, Pennsylvania, USA. [10]Department of Engineering Mechanics, Tsinghua Univeristy, Beijing, China. [11]Department of Mechanical Engineering, University of Colorado Boulder, Boulder, Colorado, USA. [12]Departments of Civil and Environmental Engineering and Mechanical Engineering, Northwestern University, Evanston, Illinois, USA. [13]These authors contributed equally to this work. Correspondence should be addressed to B.L. (littb@mail.med.upenn.edu) or J.A.R. (jrogers@uiuc.edu).
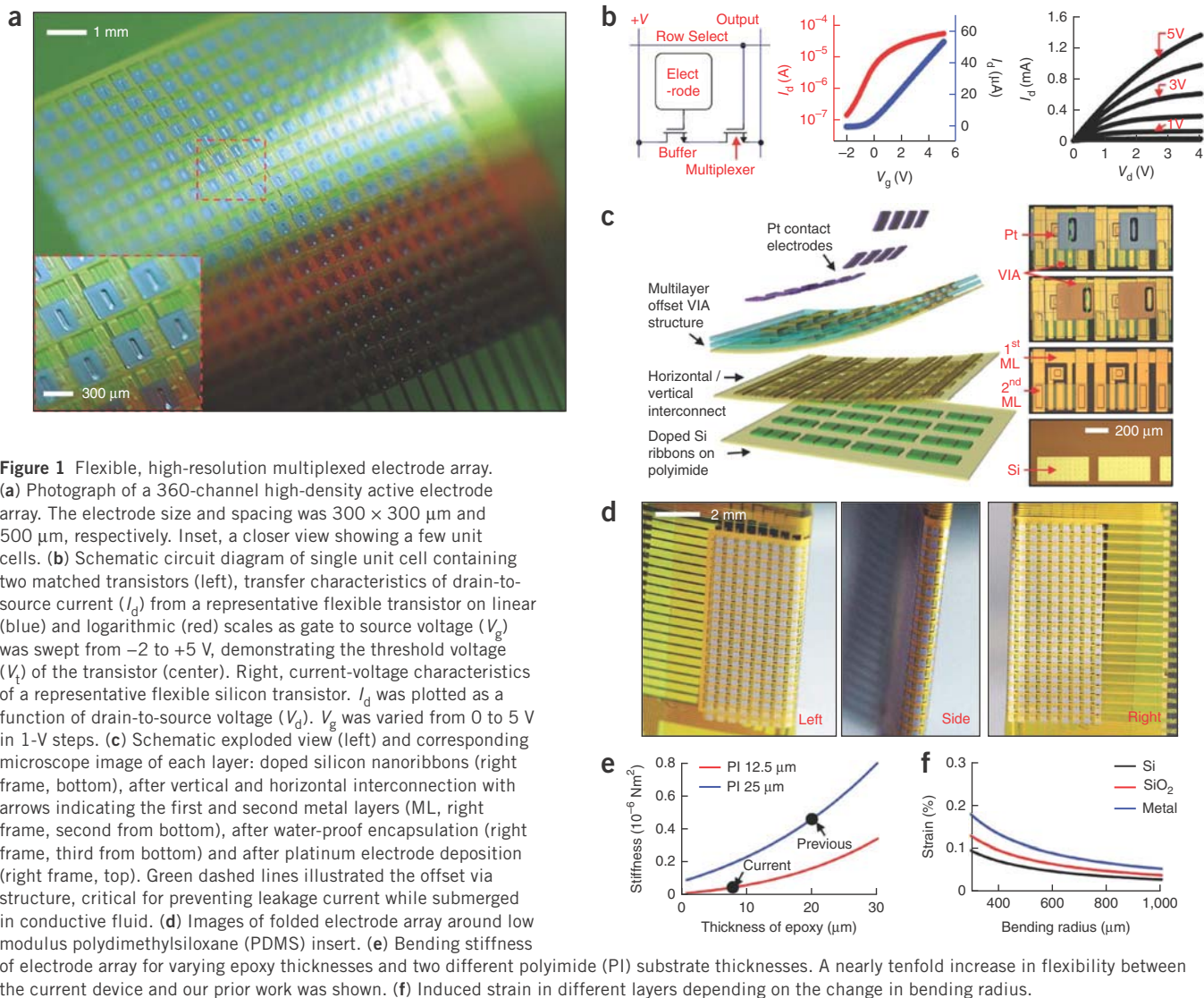
Figure 1 Flexible, high-resolution multiplexed electrode array. (**a**) Photograph of a 360-channel high-density active electrode array. The electrode size and spacing was 300 × 300 µm and 500 µm, respectively. Inset, a closer view showing a few unit cells. (**b**) Schematic circuit diagram of single unit cell containing two matched transistors (left), transfer characteristics of drain-to-source current (I_d) from a representative flexible transistor on linear (blue) and logarithmic (red) scales as gate to source voltage (V_g) was swept from −2 to +5 V, demonstrating the threshold voltage (V_t) of the transistor (center). Right, current-voltage characteristics of a representative flexible silicon transistor. I_d was plotted as a function of drain-to-source voltage (V_d). V_g was varied from 0 to 5 V in 1-V steps. (**c**) Schematic exploded view (left) and corresponding microscope image of each layer: doped silicon nanoribbons (right frame, bottom), after vertical and horizontal interconnection with arrows indicating the first and second metal layers (ML, right frame, second from bottom), after water-proof encapsulation (right frame, third from bottom) and after platinum electrode deposition (right frame, top). Green dashed lines illustrated the offset via structure, critical for preventing leakage current while submerged in conductive fluid. (**d**) Images of folded electrode array around low modulus polydimethylsiloxane (PDMS) insert. (**e**) Bending stiffness of electrode array for varying epoxy thicknesses and two different polyimide (PI) substrate thicknesses. A nearly tenfold increase in flexibility between the current device and our prior work was shown. (**f**) Induced strain in different layers depending on the change in bending radius.

RESULTS

Electrode array fabrication and testing

To enable high-resolution interface with large areas of the brain, we developed an array of flexible, nonpenetrating electrodes using flexible silicon electronics technology. The array was composed of 720 silicon nanomembrane transistors (**Fig. 1a**). The active matrix circuit design contained two transistors per unit cell (**Fig. 1b**). The buffer transistor connected to the electrode provided buffering of the biological signals, whereas the multiplexing transistor allowed all of the electrodes in the same column to share a single output wire. Flexible transistors were fabricated using high-quality single-crystal silicon, yielding a mobility of ~350 cm² V⁻¹ and an on/off ratio >10³, calculated from the slopes of the transfer curves and the ratio of maximum and minimum current outputs (**Fig. 1b**) using standard field-effect transistor models[23]. This capability enabled high-speed multiplexing (<5 µs), sampling rates >10 kS per s per electrode[24] and very low multiplexer cross-talk (<−65 dB).

Active electrode arrays were fabricated using a multi-layer process (**Fig. 1c**). Doped silicon nanomembranes, structured into ribbons with thicknesses of 260 nm, were located in the first layer through the use of transfer printing technology, as described elsewhere[24]. Subsequent horizontal and vertical metal interconnect layers were

insulated using layers of polyimide (~1.2 µm, Sigma-Aldrich). Additional polymeric encapsulation layers (polyimide and epoxy, ~1.2 µm and ~4 µm) with an offset vertical interconnect access (VIA) structure (**Fig. 1c**) prevented electrical leakage currents when the device was immersed in highly conductive bio-fluids. As a final step, platinum (~50 nm) was evaporated and deposited onto the surface electrodes to reduce their impedance (~20 kOhm at 1 kHz; detailed fabrication procedures, corresponding microscope images and a cross-sectional schematic can be found in the Online Methods and in **Supplementary Fig. 1**).

Conventional electrode technology is technically limited in its ability to record from the inside of sulci. However, implanting even a few electrodes in sulci such as the central sulcus has shown that the signals obtained carry more information for BMI applications than signals recorded from the traditional gyral surface[25]. Electrical recording from inside sulci may also be important for clinical applications, as studies of brain pathology have demonstrated that focal cortical dysplasias are preferentially located at the bottom of sulci[26]. Some devices have attempted to address this by exposing a small number of passive electrodes on both surfaces of the device[27,28], but have only achieved limited spatial sampling.

Figure 2 Animal experiment using feline model. (**a**) A flexible, high-density active electrode array was placed on the visual cortex. Inset, the same electrode array was inserted into the interhemispheric fissure. (**b**) Left, folded electrode array before insertion into the interhemispheric fissure. Right, flat electrode array inserted into the interhemispheric fissure.


The extreme flexibility of our device allowed it to be folded around ~700-µm-thick silicone rubber, forming a unique, high-resolution, double-sided recording device that allowed access to rarely explored cortical areas, such as the interior of sulci or the medial aspects of the cerebral hemispheres (**Fig. 1d**). To minimize induced strain in the silicon, silicon dioxide and metal interconnection layers during folding, we reduced the overall array thickness from 76 µm[24] to 25 µm, resulting in a nearly tenfold reduction in bending stiffness. This was accomplished by reducing the polyimide substrate thickness from 25 µm to 12.5 µm, and by reducing the epoxy encapsulation thickness from 20 µm to 8 µm (**Fig. 1e**). The induced strain in each layer during folding was estimated via analytical modeling (**Fig. 1f**) and was maintained well below the mechanical fracture strain of each inorganic material (~1% for Si and SiO_2)[29].

In vivo experiments

We used our flexible electrode device to map neural activity at high resolution on the surface of visual cortex of ten cats *in vivo* (**Fig. 2a**). An initial craniotomy and durotomy exposed a 2 × 3 cm region of cortex. Eyes were focused on a monitor that subtended 28 × 22° of space. The electrode arrays were either placed on the brain or inserted into the interhemispheric fissure (**Fig. 2a,b**). Given the high flexibility of
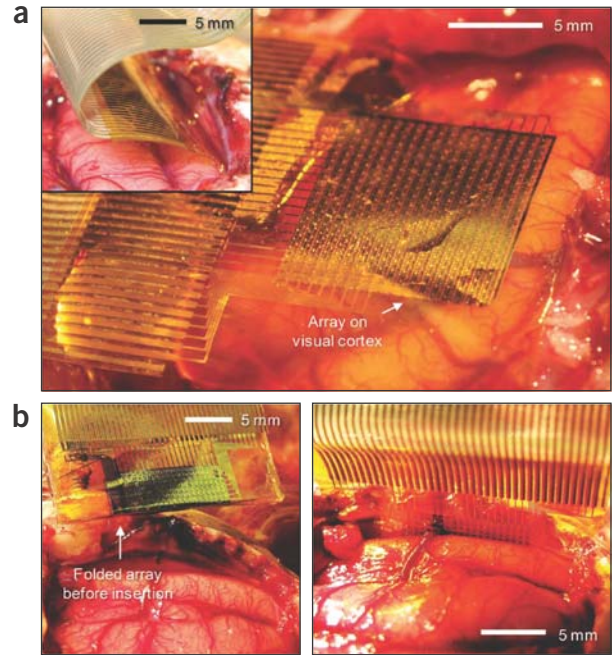
the electrode array, it could be placed in between the two hemispheres of the brain without causing damage to tissue. In this configuration, the recording surface is facing the left hemisphere. Alternately, the folded electrode array can be inserted in the same location as the flat electrode array (**Fig. 2b**), simultaneously recording from both hemispheres, with the right hemisphere filtered through the dura.
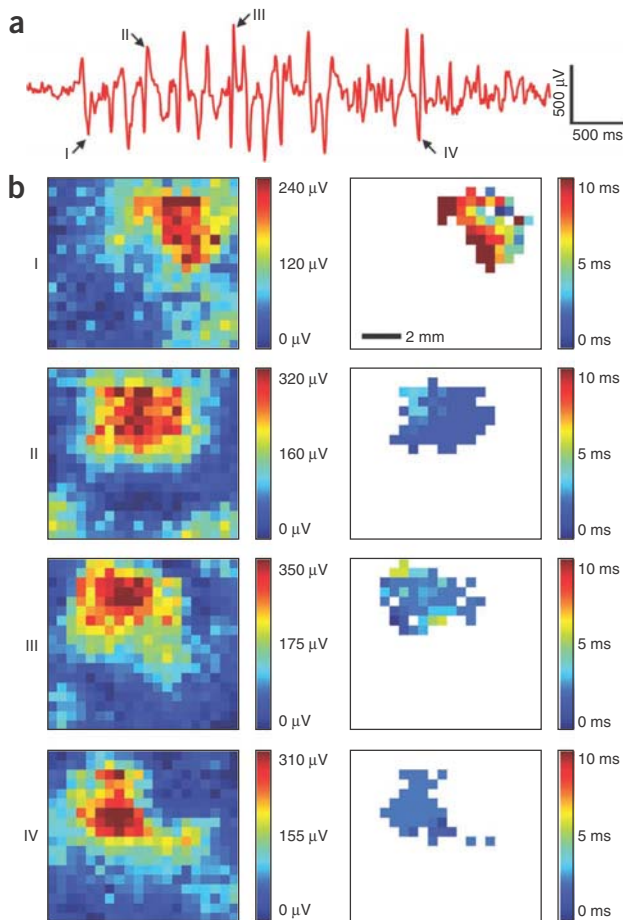
Sleep spindles

We recorded spontaneous spindles during barbiturate anesthesia in the µECoG signal. Spindle oscillations consisted of waves repeating at 5–7 Hz, lasting 1–2 s and repeating every 6–10 s. Given the large number of channels on the electrode array and the large number of spindles recorded, data from a representative channel is shown for a typical spindle (**Fig. 3a**). The signal amplitude of ~1.2 mV is consistent with earlier published reports[30]. The unfiltered noise level of 30 µV r.m.s. was greatly improved from our previous report[24]. Individual waves in spindle oscillations were identified by a detector triggered on a threshold of 2 s.d. above or below the mean. For four of these waves, the r.m.s. value of the zero-meaned signal in the 30-ms window before and after the peak was plotted on the array map (**Fig. 3b**). For each channel in the array with >50% of the maximum r.m.s. value, the time to the peak of the wave was plotted (**Fig. 3b**). We observed individual spindle waves to be spatially confined to a small region of brain (<5 × 5 mm) and they did not move. Spindle waves were highly synchronous, peaking in a few milliseconds in all of the channels that were involved.

Figure 3 Spontaneous barbiturate-induced sleep spindles. (**a**) A typical spindle recorded from a representative channel. Negative is plotted up by convention. Arrows point to individual spikes of the spindle (I–IV) that were further analyzed. (**b**) r.m.s. value of the zero-meaned signal of individual sharply contoured waves comprising the spindle revealed the high sensitivity of the electrode array and the spatially localized nature of spindles (left column), as well as the high degree of temporal synchronization indicated by the relative time to peak across the array (right column). Data are anatomically orientated as shown in the inset of **Figure 4b**.

Figure 4 Visual evoked response analysis to a two-dimensional sparse noise visual stimulus. (**a**) 64-color maps, each showing the response (r.m.s. value of the zero-meaned signal in the response window) of the entire 360-channel electrode array. The color maps are arranged in the same physical layout as the stimuli were presented on the monitor, that is, the image map in the upper left-hand corner of the figure represents the neural response across the entire array to a flashing box presented in the upper left-hand corner of the monitor. The color scale is constant over all 64 image maps and is saturated at the 1st and 99th percentile to improve the visual display. (**b**) 64-color maps generated from the same response data as in **a**, but plotting the response latency. Channels that did not show a strong response, as determined by exceeding 50% of the maximum evoked response, were excluded and are colored white. Inset, exploded view illustrates the anatomical orientation of the electrode array on the brain and approximate location of Brodmann's areas (gray numbers and dashed lines). The electrode color map data is oriented such that the bottom left-hand corner of the electrode array was approximately located over Brodmann area 18, the bottom right-hand corner over area 17, the middle region over areas 18 and 19, the upper right-hand corner over area 21 and upper left-hand corner over area 7. (**c**) Performance results achieved after subjecting a test set of data to a DBN classifier in accurately determining each originating location on the screen of respective stimuli. 23 of the 64 screen locations (36%) were predicted exactly correct (black boxes), significantly better than chance (binomial distribution, $n = 64$, $p = 1/64$, $P(x > 22) \ll 0.0001$). 42 of 64 (66%) screen locations were predicted correctly in one neighboring square (gray boxes, distance $\leq \sqrt{2}$, chance level 11.8%).
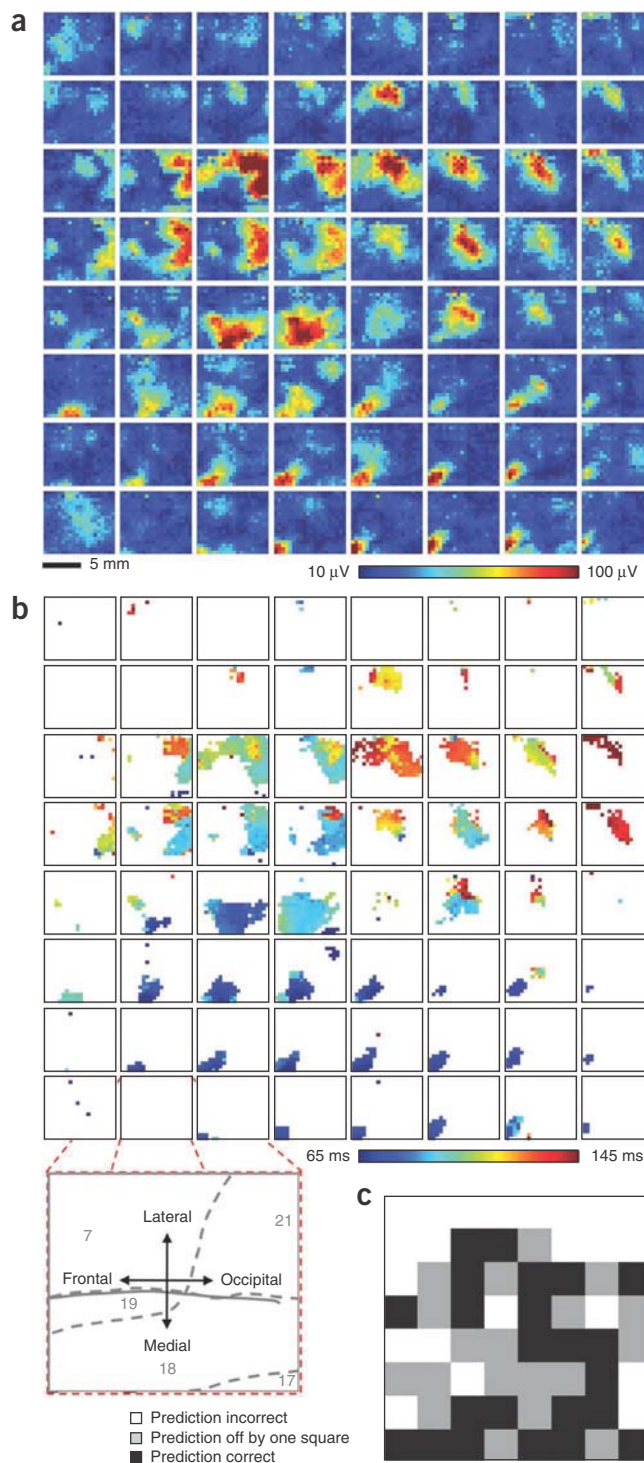
Visual evoked responses

Visual stimuli consisting of full-field drifting gratings were presented for 504 ms at 2 Hz with a spatial frequency of 0.5 cycles per degree. Single-trial visual evoked potentials[31] were visible on many channels of the electrode array (a small subset of these potentials are shown, without averaging, to illustrate the quality of the electrode array recordings; **Supplementary Fig. 2**).

A second visual stimulus consisted of flashing white boxes at pseudo-random locations in an 8 × 8 grid was presented to measure the retinotopic organization of the recorded cortical area. The duration of each flash was 200 ms, followed by a 64-ms blank time. Stimuli were presented 15 times at each location, for a total of 960 stimulus presentations. Responses from the 15 trials were averaged. The response strength for the 64 different stimulus locations was determined for each of the 360 electrode array channels by calculating the r.m.s. value of the zero-meaned signal in the 40–160-ms window after presentation of the visual stimulus, to capture the majority of the visual evoked potential[31] (**Fig. 4a**). The responses indicate that distinct regions of the brain responded to distinct areas of the visual field, as expected.

For each channel in the array with a response >50% of the peak r.m.s. value (as calculated above), the delay to the peak of the evoked response was determined (**Fig. 4b**). A few general observations are visible in the data. Stimuli presented in the lower and left areas of the screen appeared to activate small areas of the lower left-hand corner of the electrode array, and these responses occurred earliest, consistent with early visual cortical areas[32]. Stimuli presented in middle to upper-middle areas of the visual field appeared to elicit responses in large areas of the upper middle areas of the electrode array, and these activations occurred later, consistent with visual association cortex. The upper two rows of the screen appeared to be outside of the visual field covered by the array, possibly as a result of electrode placement not covering the area striata activated during stimulation at the upper portion of the visual field.

As a more rigorous test of the ability of the electrode array to resolve the visual field, we used the evoked response data to train a deep belief net (DBN) classifier[33,34]. A training set was generated by randomly

selecting 10 of the 15 trials, averaging the evoked responses and repeating this process 100 times for each of the 64 screen locations to yield 6,400 total samples. The evoked response feature vectors were calculated as described above and concatenated, giving 720 feature dimensions in each of the 6,400 samples. The trained DBN was tested on a separate dataset of ten trials, averaged together, from the same animal and recording day (**Fig. 4c**). We found that 23 of the 64 screen locations (36%) were predicted exactly correct, significantly better than chance (binomial distribution, $n = 64$, $p = 1/64$, $P(x > 22) \ll 0.0001$), and 42 of 64 (66%) screen locations were predicted correctly within 1 neighboring
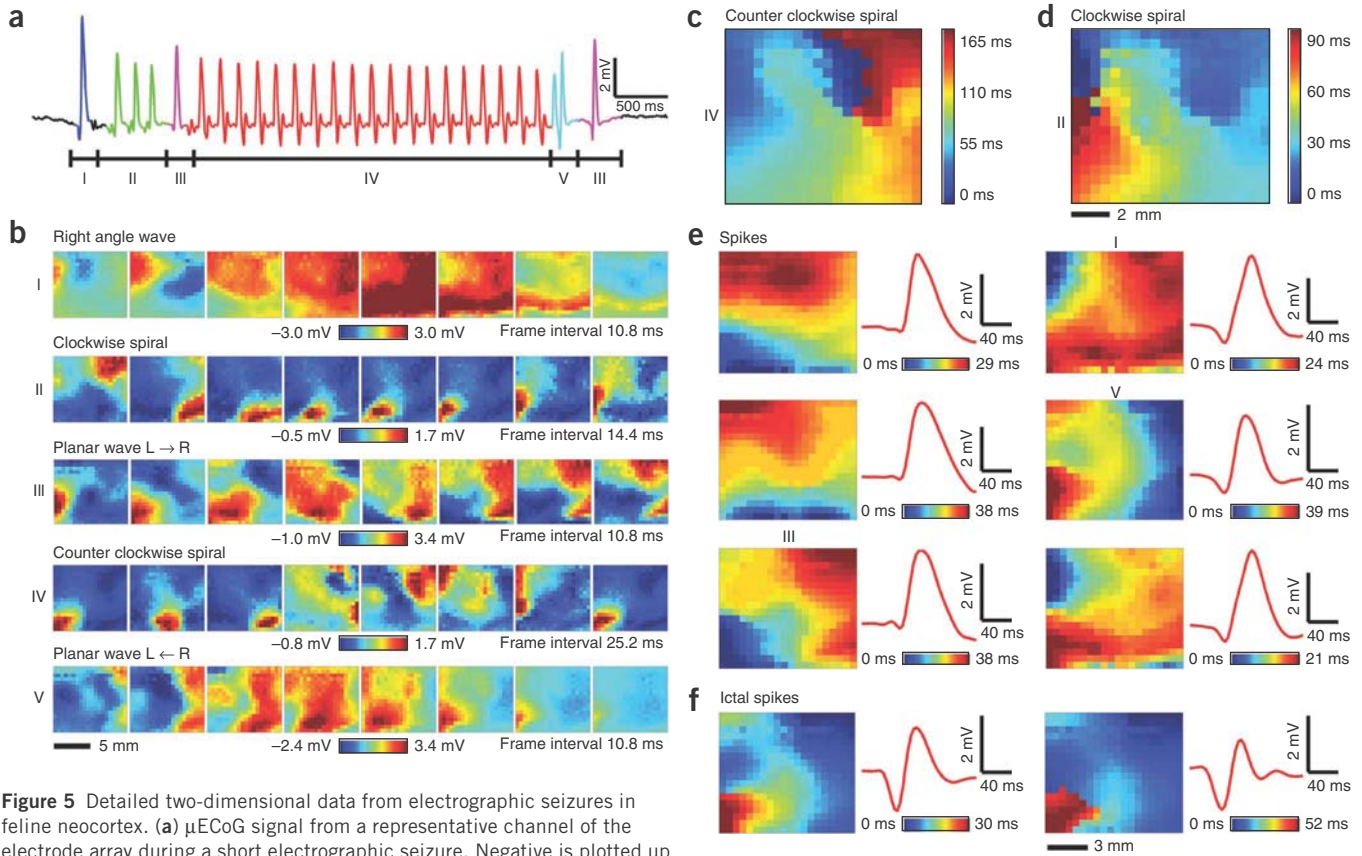
Figure 5 Detailed two-dimensional data from electrographic seizures in feline neocortex. (**a**) µECoG signal from a representative channel of the electrode array during a short electrographic seizure. Negative is plotted up by convention. Labeled segments correspond to movie frames below. (**b**) Movie frames show varied spatial-temporal µECoG voltage patterns from all 360 electrodes during the labeled time intervals from **a**. The frame interval and color scale are provided for each set of eight movie frames and the color scale is saturated at the 2nd and 98th percentile over eight frames to improve the visual display. Data are anatomically orientated as shown in the inset of **Figure 4b**. (**c**) Relative delay map for the 4–8 Hz band-pass filtered data from 3 s of continuous clockwise spiral rotations (**b**, waveform IV) illustrating a clear phase singularity and counter clockwise rotation. (**d**) Relative delay map for narrow band-pass filtered data from ~0.5 s of clockwise spiral rotations (**b**, waveform II) illustrating clockwise rotation, but a less clear singularity. (**e**) Representative delay image maps from six different spike clusters are shown to illustrate the differences between clusters (left columns). The average waveform for the corresponding spike (red traces, right columns) illustrates that complicated spatial patterns at the micro scale (0.5 mm) can be indistinguishable at the current clinical scale (~10 mm). Numerals I, III and V indicate the clusters that the corresponding waves in **b** belong to. (**f**) Representative delay image maps from two clusters that occurred almost exclusively during seizures, illustrating striking differences in spatial-temporal micro-scale patterns during seizures.

square (distance $\leq \sqrt{2}$, chance level = 11.8%). These results validate the capability of the electrode array to resolve visual evoked responses.

Electrographic seizures

As a third demonstration of this new technology, we induced seizures in the feline model using local administration of picrotoxin. The drug was placed directly on the brain, adjacent to the electrode array on the frontal-medial corner. In one of the animal experiments, the electrode array recorded four spontaneous electrographic seizures and hundreds of interictal spikes over ~1 h. The µECoG signal from a single channel of the electrode array during a short electrographic seizure (**Fig. 5a**) revealed a large amplitude (6.6 mV), low noise (45 µV r.m.s.) and high signal-to-noise ratio (SNR, 34 dB).

The array recorded spatial patterns that have not been previously observed during seizures (**Supplementary Movie 1**). At the ictal onset, there was a plane wave (**Fig. 5b**) coming from the upper left that encountered a phase anisotropy, bent to the right, and anticipated the subsequent clockwise spiral. This spiral pattern rotated for three cycles. A second incoming plane wave changed the direction of rotation of the spiral. The ensuing counterclockwise spiral rotated for 19 cycles and was terminated by a plane wave coming from the right.

On the basis of these early observations, it is possible that neocortical seizures may be initiated by interictal spikes that are diverted asymmetrically around regional anisotropies, resulting in sustained re-entrant loops. Seizures may be terminated by mutual annihilation of a rotating spiral with a traveling wave, which has implications for electrical stimulation to disrupt seizures[35]. Analogous anisotropies and colliding waves have been observed in the genesis and termination of cardiac arrhythmias[36].

Band-pass filtering the spiral wave data to investigate only the primary frequency component (as in previous analysis[37–39]) yielded delay plots that are consistent with spiral waves. The primary frequency of the counter-clockwise spiral during the seizure was 6 Hz (**Supplementary Fig. 3**). Spiral wave data was band-pass filtered from 4 to 8 Hz using a sixth-order butterworth band-pass filter in the forward and reverse directions, resulting in zero-phase distortion digital filtering (and effectively doubling the order of the filter to a 12th-order filter). The relative delay for each electrode was calculated by first upsampling by a factor of 12 and then taking the index of the maximum cross-covariance between each channel and the average of all 360 channels. The resulting delay image map (**Fig. 5c**) revealed a singularity, as if forming a counterclockwise rotating

pinwheel. Clockwise motion was also demonstrated by the delay plot (**Fig. 5d**), albeit with a less clear singularity.

In addition to the spatiotemporal patterns analyzed above, the large SNR of the electrode array allowed us to analyze the pattern of single ictal and interictal spikes. Stereotyped, repetitive spatiotemporal patterns of single spikes were frequently observed throughout the dataset. We developed a clustering algorithm to test whether the spatiotemporal patterns of single spikes could be classified consistently. First, a standard, threshold-based spike detector was run on the average of all 360 channels to provide event detections. Other methods that leverage signal detection in individual channels may allow better resolution of more localized spikes. The threshold was set at −500 μV with a refractory period of 160 ms, yielding a spike amplitude of 2.2 ± 0.95 mV (mean ± s.e.m.). The noise amplitude of the averaged signal from all 360 channels was 39 or 14 μV r.m.s. Data from all 360 electrodes in the window 60 ms before and 100 ms after the threshold crossing were upsampled by a factor of 12 and cross-correlated with the average of all 360 channels. The relative delay of the spike on each channel was calculated using the index of the maximum cross-covariance value. Upsampling allowed the relative delays to be computed with subsample time accuracy. In addition, the magnitude of the spike on each channel was calculated using the r.m.s. value of the zero-meaned signal in the same window. The 360-element delay and r.m.s. vectors representing each spike were normalized by dividing by their maximum respective values and concatenated. Using these two features, relative delay and r.m.s., the speed and direction of the wavefront, as well as its amplitude, could be encoded.

To lessen the computational burden before clustering, we used principal components analysis to reduce the dimensionality of the spike data from 720 to 81, a number of coefficients that accounted for 99% of the data variance. Finally, k-medoids clustering[40] was carried out on 877 detected spikes. The potential number of clusters, k, ranged from 1 (that is, no clustering) to 30, and the gap statistic[41] was then used to determine the optimal number of clusters[42], with 21 clusters being returned. Delay maps for all of the spikes in each cluster indicated a strong similarity in clusters (see **Supplementary Figs. 4–14**).

We plotted example relative delay image maps for six different clusters (**Fig. 5e**). The events in the six clusters were found both ictally and interictally. These examples illustrate that vastly different micro-scale spatial patterns can be indistinguishable on a macro-scale, again strongly motivating recordings from brain at high spatial resolution.

Of the 21 clusters, 5 clusters appeared to occur only during seizures (**Fig. 5f**). These results suggest that μECoG can differentiate ictal from interictal patterns that show up as nearly identical spikes at the resolution of clinical ECoG.

DISCUSSION

The electrode arrays in use today can either sample broad regions of the brain (~80 × 80 mm) at low spatial resolution (~10-mm spacing) or small regions of brain (~4 × 4 mm) at high spatial resolution (~400-μm spacing)[11], with both requiring N wires for N electrodes. We developed a 360-channel active electrode array that is capable of sampling a fivefold larger region of brain (10 × 9 mm) than previous methods[11], with high spatial resolution (500-μm spacing) and high temporal resolution (>10 kS s^{-1}) while reducing the number of wires ninefold. This technology offers spatial resolution approaching that of voltage-sensitive dyes, with greatly improved temporal resolution and SNR, with the ability to record from non-planar and non-optically accessible areas and in a potentially fully implantable, nontoxic, clinical-scale system. This technology can be rapidly scaled to clinical sizes (~80 × 80 mm) with 25,600 channels while maintaining high

temporal resolution (>1.2 kS s^{-1}), enabling the elucidation of micro-scale brain dynamics in human normal brain activity and disease.

Spiral activity has been described by mathematical models of two-dimensional excitable media[43] and has been documented in brain and heart[36–39], but until now a tool did not exist to record exhaustive spatio-temporal patterns of brain activity in a large mammalian brain. Our results suggest that spiral waves are present during seizures, although the seizures produced in this case were induced by acute disinhibition and may not accurately represent activity characterizing spontaneous seizures in chronic epilepsy. Perhaps more importantly, our technology offers a method for recording this kind of activity chronically in awake, behaving animals and humans with unprecedented detail.

The importance of high-density, active array technology is evident in the neural dynamics that emerge at a spatial scale 400-fold finer than that used clinically. This technology demonstrated complex spatial patterns, such as spiral waves, clustering of spatiotemporal patterns, and heterogeneity and anisotropy of sleep oscillations, all of which occurred in the space occupied by one current clinical ECoG electrode. Coarse spatial undersampling prevents current technology from resolving the micro-scale spatial patterns that occur in the brain, but the high resolution of this active array technology enabled us to distinguish intrinsic from pathologic signals efficiently, even in the same frequency bands.

Our observations suggest that spindles are spatially punctate, stationary and temporally coherent, whereas epileptiform activity in this model propagated as planar and spiral waves. Further research is needed to fully characterize these results and their importance. Prior investigations using voltage-sensitive dyes have found spiral waves in rodents during ECoG epochs dominated by sleep-like delta frequencies[39]; in contrast, we found activity that was spatially inhomogeneous and did not spiral, but was present during delta-dominant states and that appeared as sleep spindles electrographically. Although optical imaging has demonstrated spatial patterns, such as planar waves and spirals in disinhibited rat cortex[38], high-density, active array technology enabled us to show that these spiral dynamics in disinhibited cat cortex are electrographic seizures at the clinical scale.

Ultimately, the question of clinical relevance is whether there are spiral waves in human cortex, but voltage-sensitive dye recordings are infeasible for use in humans, as the brain needs to be optically exposed and subjected to toxic dyes. Our results suggest that technology incorporating flexible, high-density active arrays of electrodes can provide equal or superior recordings in a fully implantable system. If spiral waves are observed in human cortex, the clinical implications will be profound. Seizure control may be analogous to the control of cardiac arrhythmias, which are also known to manifest as re-entrant spiral waves of excitation[36]. Furthermore, as learning tasks increase spindle activity[44], which may be a result of consolidation and integration of memories[45], understanding the fine structure of spindles has implications for learning and memory efficiency, as well as thalamocortical networks involved in sleep and primary generalized epilepsy.

Finally, flexible devices such as those shown here hold the promise to enable neuroprosthetic devices that have been limited until now by the lack of resolution of the BMI and by the irregular topography of the brain. Using the extreme flexibility of active electrode arrays, devices can be folded and implanted into currently inaccessible brain regions, such as sulci and fissures, which can be simultaneously recorded and stimulated, along with surface regions to enable devices to facilitate movement, sensation, vision, hearing and cognition. These devices can also be powered remotely through wireless power transmission techniques[46].

Our work also has implications for treating disease. Disorders such as epilepsy, dementia, affective disorders, movement disorders and

schizophrenia are all conditions that affect dispersed brain networks, rather than a single locus of brain function. Investigations of major depression, parkinsonism and chronic pain with magnetoencephalography have identified thalamocortical dysrhythmia, but increases of spatial and temporal resolution would allow a more detailed characterization of these diseased networks[47]. Only with new approaches that can resolve micro-scale activity over large areas of cortex will we be able to begin to understand how the brain functions in both disease and health, and to develop better diagnostic and therapeutic options for those affected.

METHODS

Methods and any associated references are available in the online version of the paper at http://www.nature.com/natureneuroscience/.

Note: Supplementary information is available on the Nature Neuroscience website.

1. Freeman, W.J. Spatial spectral analysis of human electrocorticograms including the alpha and gamma bands. *J. Neurosci. Methods* **95**, 111–121 (2000).
2. Kellis, S.S., House, P.A., Thomson, K.E., Brown, R. & Greger, B. Human neocortical electrical activity recorded on nonpenetrating microwire arrays: applicability for neuroprostheses. *Neurosurg. Focus* **27**, E9 (2009).
3. Kellis, S. *et al.* Decoding spoken words using local field potentials recorded from the cortical surface. *J. Neural Eng.* **7**, 056007 (2010).
4. Kitzmiller, J.P. *et al.* Micro-field evoked potentials recorded from the porcine sub-dural cortical surface utilizing a microelectrode array. *J. Neurosci. Methods* **162**, 155–161 (2007).
5. Schevon, C.A. *et al.* Microphysiology of epileptiform activity in human neocortex. *J. Clin. Neurophysiol.* **25**, 321–330 (2008).
6. Stead, M. *et al.* Microseizures and the spatiotemporal scales of human partial epilepsy. *Brain* **133**, 2789–2797 (2010).
7. Amunts, K., Malikovic, A., Mohlberg, H., Schormann, T. & Zilles, K. Brodmann's areas 17 and 18 brought into stereotaxic space-where and how variable? *Neuroimage* **11**, 66–84 (2000).
8. Branco, D.M. *et al.* Functional variability of the human cortical motor map: electrical stimulation findings in perirolandic epilepsy surgery. *J. Clin. Neurophysiol.* **20**, 17–25 (2003).
9. Fox, P.T. *et al.* Location-probability profiles for the mouth region of human primary motor-sensory cortex: model and validation. *Neuroimage* **13**, 196–209 (2001).
10. Van Essen, D.C., Newsome, W.T. & Maunsell, J.H. The visual field representation in striate cortex of the macaque monkey: asymmetries, anisotropies, and individual variability. *Vision Res.* **24**, 429–448 (1984).
11. Campbell, P.K., Jones, K.E., Huber, R.J., Horch, K.W. & Normann, R.A. A silicon-based, three-dimensional neural interface: manufacturing processes for an intracortical electrode array. *IEEE Trans. Biomed. Eng.* **38**, 758–768 (1991).
12. Hochberg, L.R. *et al.* Neuronal ensemble control of prosthetic devices by a human with tetraplegia. *Nature* **442**, 164–171 (2006).
13. Ryu, S.I. & Shenoy, K.V. Human cortical prostheses: lost in translation? *Neurosurg. Focus* **27**, E5 (2009).
14. Polikov, V.S., Tresco, P.A. & Reichert, W.M. Response of brain tissue to chronically implanted neural electrodes. *J. Neurosci. Methods* **148**, 1–18 (2005).
15. Schmidt, S., Horch, K. & Normann, R. Biocompatibility of silicon-based electrode arrays implanted in feline cortical tissue. *J. Biomed. Mater. Res.* **27**, 1393–1399 (1993).
16. Griffith, R.W. & Humphrey, D.R. Long-term gliosis around chronically implanted platinum electrodes in the Rhesus macaque motor cortex. *Neurosci. Lett.* **406**, 81–86 (2006).
17. Margalit, E. Visual and electrical evoked response recorded from subdural electrodes implanted above the visual cortex in normal dogs under two methods of anesthesia. *J. Neurosci. Methods* **123**, 129–137 (2003).
18. Chao, Z.C., Nagasaka, Y. & Fujii, N. Long-term asynchronous decoding of arm motion using electrocorticographic signals in monkeys. *Front. Neuroeng.* **3**, 3 (2010).
19. Yeager, J.D., Phillips, D.J., Rector, D.M. & Bahr, D.F. Characterization of flexible ECoG electrode arrays for chronic recording in awake rats. *J. Neurosci. Methods* **173**, 279–285 (2008).
20. Andersen, R.A., Musallam, S. & Pesaran, B. Selecting the signals for a brain-machine interface. *Curr. Opin. Neurobiol.* **14**, 720–726 (2004).
21. Mehring, C. *et al.* Inference of hand movements from local field potentials in monkey motor cortex. *Nat. Neurosci.* **6**, 1253–1254 (2003).
22. Brunner, P., Ritaccio, A.L., Emrich, J.F., Bischof, H. & Schalk, G. Rapid communication with a "P300" matrix speller using electrocorticographic signals (ECoG). *Front. Neurosci.* **5**, 5 (2011).
23. Streetman, B.G. & Banerjee, S.K. *Solid State Electronic Devices* (Pearson, 1981).
24. Viventi, J. *et al.* A conformal, bio-interfaced class of silicon electronics for mapping cardiac electrophysiology. *Sci. Transl. Med.* **2**, 24ra22 (2010).
25. Yanagisawa, T. *et al.* Neural decoding using gyral and intrasulcal electrocorticograms. *Neuroimage* **45**, 1099–1106 (2009).
26. Besson, P., Andermann, F., Dubeau, F. & Bernasconi, A. Small focal cortical dysplasia lesions are located at the bottom of a deep sulcus. *Brain* **131**, 3246–3255 (2008).
27. Stieglitz, T. Flexible biomedical microdevices with double-sided electrode arrangements for neural applications. *Sens. Actuators A Phys.* **90**, 203–211 (2001).
28. Stieglitz, T. Flexible BIOMEMS with electrode arrangements on front and back side as key component in neural prostheses and biohybrid systems. *Sens. Actuators B Chem.* **83**, 8–14 (2002).
29. Thompson, S.E. *et al.* A 90-nm logic technology featuring strained-silicon. *IEEE Trans. Electron. Dev.* **51**, 1790–1797 (2004).
30. Kim, D.-H. *et al.* Dissolvable films of silk fibroin for ultrathin conformal bio-integrated electronics. *Nat. Mater.* **9**, 511–517 (2010).
31. Padnick, L.B. & Linsenmeier, R.A. Properties of the flash visual evoked potential recorded in the cat primary visual cortex. *Vision Res.* **39**, 2833–2840 (1999).
32. Tusa, R.J., Rosenquist, A.C. & Palmer, L.A. Retinotopic organization of areas 18 and 19 in the cat. *J. Comp. Neurol.* **185**, 657–678 (1979).
33. Hinton, G.E. & Salakhutdinov, R.R. Reducing the dimensionality of data with neural networks. *Science* **313**, 504–507 (2006).
34. Larochelle, H., Erhan, D., Courville, A., Bergstra, J. & Bengio, Y. An empirical evaluation of deep architectures on problems with many factors of variation. *Proc. Int. Conf. Mach. Learn.* 473–480 (2007).
35. Anderson, W.S., Kudela, P., Cho, J., Bergey, G.K. & Franaszczuk, P.J. Studies of stimulus parameters for seizure disruption using neural network simulations. *Biol. Cybern.* **97**, 173–194 (2007).
36. Witkowski, F.X. *et al.* Spatiotemporal evolution of ventricular fibrillation. *Nature* **392**, 78–82 (1998).
37. Prechtl, J.C., Cohen, L.B., Pesaran, B., Mitra, P.P. & Kleinfeld, D. Visual stimuli induce waves of electrical activity in turtle cortex. *Proc. Natl. Acad. Sci. USA* **94**, 7621–7626 (1997).
38. Huang, X. *et al.* Spiral waves in disinhibited mammalian neocortex. *J. Neurosci.* **24**, 9897–9902 (2004).
39. Huang, X. *et al.* Spiral wave dynamics in neocortex. *Neuron* **68**, 978–990 (2010).
40. Hastie, T., Tibshirani, R. & Friedman, J. *The Elements of Statistical Learning.* (Springer-Verlag, New York, 2001).
41. Tibshirani, R., Walther, G. & Hastie, T. Estimating the number of clusters in a data set via the gap statistic. *J. R. Stat. Soc. Series B Stat. Methodol.* **63**, 411–423 (2001).
42. Blanco, J.A. *et al.* Unsupervised classification of high-frequency oscillations in human neocortical epilepsy and control patients. *J. Neurophysiol.* **104**, 2900–2912 (2010).
43. Paullet, J.E. & Ermentrout, G.B. Stable rotating waves in two-dimensional discrete active media. *SIAM J. Appl. Math.* **54**, 1720 (1994).
44. Gais, S., Mölle, M., Helms, K. & Born, J. Learning-dependent increases in sleep spindle density. *J. Neurosci.* **22**, 6830–6834 (2002).
45. Tamminen, J., Payne, J.D., Stickgold, R., Wamsley, E.J. & Gaskell, M.G. Sleep spindle activity is associated with the integration of new memories and existing knowledge. *J. Neurosci.* **30**, 14356–14360 (2010).
46. Sekitani, T. *et al.* A large-area wireless power-transmission sheet using printed organic transistors and plastic MEMS switches. *Nat. Mater.* **6**, 413–417 (2007).
47. Llinás, R.R., Ribary, U., Jeanmonod, D., Kronberg, E. & Mitra, P.P. Thalamocortical dysrhythmia: A neurological and neuropsychiatric syndrome characterized by magnetoencephalography. *Proc. Natl. Acad. Sci. USA* **96**, 15222–15227 (1999).

ONLINE METHODS

Fabrication of the active electrode array. Doped silicon nano-ribbons on a silicon-on-insulator wafer (Si(260 nm)/SiO$_2$(1,000 nm)/Si; SOITEC) were prepared using a high-temperature diffusion process (950–1,000 °C) in a rapid thermal annealing system. These nano-ribbons were transfer printed onto a polyimide substrate (12.5 µm, Kapton) using spin-coated, uncured polyimide as a glue layer. Once the polyimide was cured, gate oxide was deposited with plasma-enhanced chemical vapor deposition (Plasmatherm). Contact openings for the source and drain connects were made with a buffered oxide etchant (Transene). Finally, metal (Cr/Au, 5 nm/150 nm) was deposited using an electron beam evaporator (Temescal), creating n-type transistor arrays. Each unit cell contained two transistors, which were connected by metal lines. Subsequent layers of metal interconnections were electrically isolated with polymeric interlayer dielectric (1.2 µm, polyimide, Sigma-Aldrich). Following two metal circuit interconnection layers, a water-proof encapsulation was formed with a photocurable epoxy (SU8, Microchem), protecting the device while it was submerged in conductive bio-fluids. The completed active sensor array was connected to an interface circuit board through a flexible anisotropic conductive film (Elform).

Multiplexing. The connections between four unit cells are illustrated in **Supplementary Figure 15**. When connected to an external constant current sink, the selected unit cell completes the current path from +V to −V and forms a source-follower amplifier. The buffered voltage output is from the same circuit node that is connected to the constant current sink. The 18-row select signals of the multiplexed electrode array were cycled at 5 kHz to sample all of the electrodes on the array, yielding a sampling rate of ~277 Hz per active electrode, with all 18 electrodes in a given column being sampled sequentially. The multiplexer output settled in less than 5 µs, allowing the row select signals to be cycled at >200 kHz. With faster analog-to-digital converters, the electrode sampling rate can be readily increased to >10 kS s^{-1} per electrode without loss of SNR[24], as validated using an analog-to-digital converter capable of sampling at 1 MS s^{-1}.

Data acquisition. The multiplexed analog signals were synchronously sampled at 100 kS s^{-1} using a custom data acquisition system (see **Supplementary Figs. 16–25**). We used 20-fold oversampling per switch interval to improve the SNR (yielding the 5-kHz cycling rate). Voltage data were recorded from all 360 electrodes of the active electrode array. The reference (ground) electrode for the acquisition system was clipped to nearby exposed muscle. Except where otherwise indicated, the µECOG data for all experiments were band-pass filtered from 1 to 50 Hz using a sixth order butterworth band-pass filter in the forward and reverse directions, resulting in zero-phase distortion digital filtering (and effectively doubling the order of the filter to a 12th-order filter).

Animal experiments. Experiments were conducted in accordance with the ethical guidelines of the US National Institutes of Health and with the approval of the Institutional Animal Care and Use Committee of the University of Pennsylvania. Surgical and stimulation methods were described in detail previously[48,49]. Briefly, adult cats (2.5–3.5 kg) were anesthetized with intravenous thiopental with a continuous infusion (3–10 mg per kg of body weight per h) and paralyzed with gallamine triethiodide (Flaxedil). Heart rate, blood pressure, end-tidal CO$_2$ and EEG were monitored throughout the experiment to assure depth and stability of anesthesia and rectal temperature was kept at 37–38 °C with a heating pad. The surface of the visual cortex was exposed with a craniotomy.

During visual stimulation, the corneas were protected with contact lenses after dilating the pupils with 1% ophthalmic atropine (wt/vol) and retracting the nictitating membranes with phenylephrine (Neosynephrine). Spectacle lenses were chosen by the tapetal reflection technique to optimize the focus of stimuli on the retina. The position of the monitor was adjusted with an *x-y* stage so that the area centrals were centered on the screen. Stimuli were presented on an Image Systems model M09LV monochrome monitor operating at 125 frames per s at a spatial resolution of 1,024 × 786 pixels and a mean luminance of 47 cd m^{-2}.

Bending stiffness and bending strain. The cross-section of the electrode array is shown in **Supplementary Figure 1b**. As the Au (500 nm and 150 nm), Si (260 nm) and SiO$_2$ (100 nm) layers between the top SU8 and bottom Kapton are very thin, and are very close to the neutral mechanical plane, their contribution to the bending stiffness can be approximated by polyimide to within 1% error.

Thus, the complex multilayer electrode can be approximated by a two-layer structure, composed of polyimide of thickness h_2 and SU8 of thickness h_1. The distance of neutral mechanical plane from the Kapton bottom is y_0, and is obtained as

$$y_0 = \frac{\bar{E}_{PI}h_2^2 + \bar{E}_{SU8}h_1(2h_2 + h_1)}{2(\bar{E}_{PI}h_2 + \bar{E}_{SU8}h_1)} \quad (1)$$

where

$$\bar{E} = \frac{E_i}{1 - \nu_i^2}$$

relates to Young's modulus E_i and Poisson's ratio ν_i (i = PI for polyimide layer and SU8 for SU8 layer).

The bending stiffness of the electrode is

$$EI = \bar{E}_{PI}bh_2\left(\frac{1}{3}h_2^2 - h_2 y_0 + y_0^2\right) + \bar{E}_{SU8}bh_1\left(\frac{1}{3}h_1^2 + h_1(h_2 - y_0) + (h_2 - y_0)^2\right) \quad (2)$$

where b (10 mm) is the electrode width.

For the electrode bent to a radius of R, the strain at position of distance y from the Kapton bottom is

$$\varepsilon = \frac{y - y_0}{R} \quad (3)$$

Mechanics of electrode insertion. The electrode is folded around a soft PDMS of Young's modulus $E_{PDMS} = 100$ kPa, width B and thickness h_{PDMS}, and is inserted into the gap of thickness h_{gap} between the hemispheres of the brain. The insertion depth is d (see **Supplementary Fig. 26a**). As the thickness of brain (>10 mm) is much larger than that of the folded electrode (~0.7 mm), the two hemispheres of the brain are modeled as semi-infinite solids, of Young's modulus $E_{brain} = 3$ kPa and Poisson's ratio $\nu_{brain} = 0.35$ (ref. 50). For a semi-infinite solid subject to uniform pressure p at the top surface in the circular region of radius $a = \sqrt{Bd}$, the surface subsidence w at position of distance r from the circular center is

$$w = \frac{4(1 - \nu_{brain}^2)p\sqrt{Bd}\int_0^{\pi/2}\sqrt{1 - r^2 \sin^2\varphi/Bd}\,d\varphi}{\pi E_{brain}}$$

whose average over the pressure region is obtained as

$$\bar{w} = \frac{16(1 - \nu_{brain}^2)p\sqrt{Bd}}{3\pi E_{brain}} \quad (4)$$

Since the electrode array is much stiffer and thinner than PDMS, its deformation as result of insertion is negligible compared to PDMS. Thus, displacement continuity gives the relation between the pressure at the interface p and the average subsidence $\bar{w}$ of the brain surface owing to electrode insertion to be $\frac{p}{E_{PDMS}}h_{PDMS} + 2\bar{w} = h_{PDMS} - h_{gap}$, which gives

$$p = \frac{h_{PDMS} - h_{gap}}{\dfrac{h_{PDMS}}{E_{PDMS}} + \dfrac{32(1 - \nu_{brain}^2)\sqrt{Bd/\pi}}{3\pi E_{brain}}} \quad (5)$$

and the maximum compressive strain in the brain as a result of electrode insertion is obtained as

$$\varepsilon^{max} = \frac{-(1 + \nu_{brain})p}{E_{brain}}\left(1 - 2\nu_{brain} + 2\left(\frac{2\nu_{brain}}{3}\right)^{3/2}\right)$$

$$= \frac{-(1 + \nu_{brain})\left(1 - 2\nu_{brain} + 2\left(\frac{2\nu_{brain}}{3}\right)^{3/2}\right)(h_{PDMS} - h_{gap})}{\dfrac{E_{brain}}{E_{PDMS}}h_{PDMS} + \dfrac{32(1 - \nu_{brain}^2)\sqrt{Bd}}{3\pi^{3/2}}} \quad (6)$$

As the folded electrode inserts into the brain gap (insertion length d), the gap (h_{gap}) between the left and right brains decreases and approaches an asymptote $\bar{h}_{gap}$ (that is, minimal gap distance). The brain gap (h_{gap}) can be generally written as an exponentially decaying function of the rubber insertion length d, $h_{gap} = \bar{h}_{gap} + (h_{PDMS} - \bar{h}_{gap}) \exp(-d/1\text{ mm})$, which defines zero insertion length as rubber first touches the brain (that is, $h_{gap} = h_{PDMS}$). For $h_{PDMS} = 700$ μm and $B = 16.2$ mm in experiment, the maximum compressive strain in the brain versus the insertion depth of rubber is shown in **Supplementary Figure 26b** for minimal brain gaps $\bar{h}_{gap} = 500$ and 600 μm.

Circuit design. The dimensions of the two transistors in the unit cell (**Fig. 1b**) are equal so that they will have matched performance. The width of both transistors was chosen to be as large as possible at 200 μm while still leaving room for large interconnections between adjacent unit cells. The length was chosen at 20 μm to be conservative for the processing technology. The resulting width:length ratio of 10 yielded reasonable levels of current output. The width of all metal lines and size of all VIAs was increased by 2, ~4× from prior designs to improve reliability and ease manufacturing. The electrode spacing was set at 500 μm based on prior work and to match well with the 500-μm spacing of the anisotropic conductive film ribbon cable, enabling a simple layout of the interconnections.

Current sinks. The ideal current sinks shown in **Supplementary Figure 15** can be implemented using commercially available semiconductors as shown in the block diagram in **Supplementary Figure 17**. This basic circuit is implemented 20 times, one for each column of the electrode array. The circuit makes use of several commercial semiconductors. The first of which is the LM334, which is a 3-terminal adjustable current source (National Semiconductor). It is used to set the constant current for the source follower. The current is adjusted via a potentiometer on the third pin (data not shown). The constant current generated by the LM334 is mirrored by the current mirror section of the REF200, current reference (Texas Instruments). The REF200 is used because the LM334 cannot respond to fast transients while supplying low amounts of current. The REF200 current mirror bandwidth is 5 MHz, to enable fast multiplexing. The REF200 also contains two 100-μA constant current sources, which are not used.

The output of a single column from the electrode array is connected to the current mirror and the non-inverting input of a TLC2274 Op Amp as shown. The TLC2274 Op Amp (Texas Instruments) is used to provide buffering for the output of the source follower amplifier. This Op Amp buffers the signal before the high-pass filter. In addition, adding this Op Amp allows the buffering to occur as close as possible to the electrode array, minimizing parasitic capacitance and maximizing the switching speed.

The output of the Op Amp is connected to a 0.01-Hz high-pass filter. This very low-frequency high-pass filter is used to remove the average direct current offset introduced by the source follower configuration of the amplifiers on the electrode array. The high-pass filter frequency must be very low because it introduces aliasing for signals up to ~0.1 Hz. Signals lower than this present on one multiplexed channel will be aliased onto the other channels. However, any aliasing that occurs can be removed by a subsequent 1-Hz digital high pass filter on the acquired data.

Data acquisition system. The output of the high-pass filter is connected using a short cable (2′) to a custom data acquisition system interface (see **Supplementary Figs. 16b,c** and **18–25**). The signal will be buffered again by another TLC2274 Op Amp to drive the 15′ cable (National Instruments) from the acquisition system interface board to a set of four PXI-6289 data acquisition cards (National Instruments). This second stage of buffering prevents any loading introduced by the long cable run from influencing the high-pass filter stage.

The data acquisition system is controlled through custom LabVIEW software (National Instruments). The data are demultiplexed in software, in real time. The first and last sample in a given multiplexer switch interval are discarded, as these samples are adjacent to the row select signal transition and are usable as a result of timing inaccuracies in the PXI-6289 analog-to-digital converter. If an over-sampling ratio greater than 3 is used, the samples that remain after discarding the first and last samples are averaged in real time, further

reducing the recorded noise. A subset of the demultiplexed channels is shown in real time during the experiment. All data are saved for later offline filtering and analysis using custom MATLAB software (MathWorks).

Gain. The gain of the electrode array was measured by submerging the array in conductive saline. A silver-wire electrode was submerged in the saline approximately 1″ from the electrode array. The second electrode was connected to a 100-mV peak-to-peak sine wave at 3.14 Hz. This test presents a uniform signal for all of the electrodes on the array to measure. The recording duration of this test was 80 s and the sampling rate was ~277 Hz per electrode. The median signal level for all 360 channels on the array was 68 mV peak-to-peak, yielding a median gain of 0.68. The gain of the array can be increased to ~1 with improvements to the biasing circuitry off of the electrode array. Substantial voltage gain is possible with alternative circuit designs.

The spatial distribution of the peak to peak amplitudes measured is shown in **Supplementary Figure 27**, illustrating the uniformity of the gain across the electrode array. Approximately 83% of the electrode channels were operational for this sample. Channels that were determined to be not operational through this test were interpolated from neighboring operational channels using a two-dimensional averaging spatial filter of window size 3 × 3 pixels before all of the analyses presented in the main text.

Power supplies. This electrode array design does not require symmetric power supplies. That is, the +V supply does not need to be equal and opposite of the −V supply. In fact, the source follower amplifier only requires that the +V supply is greater than V_{in}, the input voltage minus V_t, the threshold voltage of the amplifying transistor. Given that V_{in} is typically in the range of ± 100 mV for neural signals, as long as V_t is greater than +100 mV (typical values are ~0.7 V, **Fig. 1b**), +V can be directly connected to ground (0 V). However, if V_t of the array is small or negative, the +V supply can be connected to a separate, small positive voltage supply, such as 0.5 V.

Directly connecting the array +V connection to ground or at least minimizing the voltage of the positive supply has several advantages. The most important of which is that it reduces the potential for leakage currents through the gate of the buffer transistor (**Fig. 1b**) by reducing the voltage potential between the electrode (gate) and the silicon substrate. Another advantage is simplifying the power connections for the electrode array.

Electrode materials. The electrode base metal was gold and an additional coating of flat platinum was added to reduce the electrode impedance. Passive electrodes (250 μm × 250 μm using the same dimensions and materials processing steps) were fabricated to measure the impedance difference. Passive electrodes must be used to measure the impedance, as it is not currently possible to measure electrode impedance while integrated in the active electrode.

The mean impedance of the 250 × 250 μm passive electrodes was 84 kOhm ± 17% at 1 kHz, whereas the impedance of the same electrode design coated with flat platinum was 29 kOhm ± 9% at 1 kHz. Measurements were conducted with the array immersed in normal saline (0.9%, wt/vol). The reduced impedance provided by the platinum coating should increase the current output of the electrode and enable better signal transfer.

The electrodes in the active electrode array illustrated in **Figure 1a** are 300 μm × 300 μm. Based on linear extrapolation from prior measurements, we expect the impedance of these electrodes to be ~69% of the measured value (29 kOhm) of the 250 μm × 250 μm electrodes or ~20 kOhm at 1 kHz.

The output impedance of the active electrodes are substantially lower than 20 kOhm as a result of the integrated buffer amplifier, which allows the multiplexer to settle rapidly after switching, despite driving large parasitic capacitances owing to long interface cabling.

48. Cardin, J.A., Palmer, L.A. & Contreras, D. Stimulus feature selectivity in excitatory and inhibitory neurons in primary visual cortex. *J. Neurosci.* **27**, 10333 (2007).
49. Cardin, J.A., Palmer, L.A. & Contreras, D. Cellular mechanisms underlying stimulus-dependent gain modulation in primary visual cortex neurons in vivo. *Neuron* **59**, 150–160 (2008).
50. Taylor, Z. & Miller, K. Reassessment of brain elasticity for analysis of biomechanisms of hydrocephalus. *J. Biomech.* **37**, 1263–1269 (2004).